Experimental and numerical investigation of sloshing under roll excitation at shallow liquid depths

Erlend Liavåg Grotle[a,*], Hans Bihs[b], Vilmar Æsøy[a]

[a] *Department of Maritime Technology and Operations, Norwegian University of Science and Technology (NTNU), NO-6009 Ålesund, Norway*

[b] *Department of Civil and Transport Engineering, Norwegian University of Science and Technology (NTNU), NO-7491 Trondheim, Norway*

Abstract

This paper investigates sloshing at shallow-liquid depths in a rectangular container by using experimental and numerical methods. A motion platform is used to perform a prescribed periodic rotational motion to excite the liquid sloshing at a range of frequencies and filling levels. Simulated free-surface elevation is compared with the experimental results for a selection of cases. The wave mechanisms at the chosen fillings are studied by combining numerical methods and the experimental results. We find that the simulated free-surface elevation is in close agreement with experimental results inside the resonance zone. But at frequencies above the bifurcation point, with several overlapping waves, the deviation is increasing. The bifurcation point is determined for a range of filling levels through observation. The numerical results provide important information about sloshing mechanisms at these depths. Complex interaction between the bottom, the lower layer and the wave influences the amount of dissipation before the wave hits the wall. The existing theory seems to be too conservative in predicting the occurrence of hydraulic jumps in the upper limit.

Keywords: Sloshing, experiments, RANS, shallow depths, resonance zone

1. Introduction

Sloshing can be characterized as the motion of liquids in containers or vessels. Sloshing can occur with more than one immiscible liquid, as studied in La Rocca *et al.* [1], [2]. There are several applications in which sloshing may occur. The basic problem sloshing presents is estimating the hydrodynamic pressure distribution, forces, moments, and natural frequencies. Extensive work on how to approach it analytically can be found in [3] and [4]. The former focuses on space applications, while the latter focuses on sloshing within the maritime field. Naturally, a moving ship in waves is subject to sloshing. Within the maritime field there are tanks of different applications, but in general all marine vehicles have some kind of tank installed on-board. Examples are roll-stabilizer tanks or cargo tanks carrying different type of liquids. Impact at shallow depths can cause great damage to the tank. The resonance zone extends to frequencies higher than the calculated first natural frequency. Depending on the depth, frequencies below the the first natural frequency result in a bore [5], [6]. By increasing the frequency, it is possible to cause the bore to travel all the way from one wall to the other. Further increase of the frequency results in a narrow region where a steep solitary wave travels the entire tank length without breaking, and this results in severe impact on the side walls. This paper aims to characterize wave patterns in a sloshing tank under roll and to identify frequencies that cause severe impacts at low fillings.

*Corresponding author

Email address: erlend.l.grotle@ntnu.no (Erlend Liavåg Grotle)

There are many methods to analyse sloshing and several studies use experimental or analytical approaches to examine the subject. Olsen and Johnsen [5] characterized sloshing at these depths and performed a limited number of tests with forced roll. Armenio and La Rocca [7] investigated sloshing with forced and free oscillations at shallow depths under rolling motion. The roll amplitude varies between 1.0° and 4.5° with two different depths. They compare results using the shallow water equations (SWE) form of the Navier-Stokes equations and RANS equations, and they found higher accuracy with RANS than with SWE. La Rocca *et al.* [8] and [9] also performed theoretical and experimental analysis of sloshing in a rotating container at intermediate depths. A fully nonlinear model is defined by applying the variational method. A technique to select the most energetic modes from experimental tests is presented. The comparison between experiments and theory shows good agreement.

To investigate the detailed flow conditions in sloshing, both with and without internal structures, computational fluid dynamics (CFD) provide promising capabilities. Viscous dissipation is accounted for and wave breaking regimes can be modelled with good accuracy. The literature offers several studies. Gómez-Goñi *et al.* [10] compared two CFD tools using the volume of fluid method (VOF) and a multi-modal sloshing model by Ansari *et al.* [11]. They found good agreement between the two CFD codes, but the multi-modal method over-predicted the wave amplitude in some conditions. Bai *et al.* [12] used a finite difference CFD model to simulate a full scale LNG tank undergoing realistic ship motions. To capture the free surface, a level-set method is employed. To validate the simulations, both longitudinal and rotational motions are considered. Few cases that compared free-surface elevation are considered. The comparison of pressure data showed acceptable agreement. Zhao and Chen [13] implemented a finite-analytical NavierStokes (FANS) flow solver in conjunction with a new coupled level-set and VOF method (CLSVOF). Impact pressure from simulations are compared with experimental data and shows good agreement. They also compared the method to a level-set method with global mass conservation and found that the CLSVOF method showed an significant reduction in the relative mass change.

An increasing trend is to use large-eddy simulations (LES), but this comes at a computational cost, which increases with higher Reynolds number. Liu and Lin [14] simulated sloshing in a three-dimensional tank using LES with the Smagorinsky subgrid scale model. However, their comparisons only concern non-linear sloshing conditions, excluding the resonant case. The cases with violent sloshing were not validated against experimental data.

Another method that has proven promising in predicting wave motions in sloshing is smooth particle hydrodynamics (SPH). Iglesias *et al.* [15] performed SPH simulations of passive anti-roll tanks. The phase-lag for the roll moment is compared to experimental results for different fillings and roll amplitudes. Bouscasse *et al.* [16] investigated shallow depth sloshing for sway. They compared experimental results with a δ-SPH scheme and found that the method proved to be robust and reliable in studying violent free-surface flows. An extensive experimental program is presented, with several amplitudes and fillings. An additional classification of the wave patterns by Olsen and Johnsen [5] are presented. Delorme *et al.* [17] and Bulian *et al.* [18] also compare SPH simulations and experiments.

The numerical model, REEF3D [19], [20] which we use in this work is based on discretization and solving the Reynolds-averaged Navier-Stokes equations (RANS). The novelties of the RANS simulations are the use of level-set method and the improved turbulence boundary condition at the free surface. The model has been extensively used for wave hydrodynamics problems [21], ocean wave energy [22] and sediment transport problems [23]. Forced sloshing within the proximity of the first mode natural frequency as well as free sloshing is simulated and compared to experiments performed at the lab facility at the Norwegian University of Science and Technology (NTNU) in Ålesund. Together with the high-order numerical treatment of the governing equations, this leads to high-quality simulation results, as shown through the comparison with the measured data in the first part of the paper. In the second part, investigation of the resonance zone at shallow depth sloshing is performed. The mean wave amplitude and bifurcation point is determined for a range of fillings. The combination of RANS simulations and experimental observations has led to an improved representation of the sloshing hydrodynamics.

2. Numerical model

2.1. RANS equations

The governing equations are the incompressible RANS equations given in tensor notations valid for two and three dimensions:

$$\frac{\partial \overline{u}_i}{\partial t} + \overline{u}_j \frac{\partial \overline{u}_i}{\partial x_j} = -\frac{1}{\rho}\frac{\partial \overline{p}}{\partial x_i} + \frac{\partial}{\partial x_j}\left[(\nu + \nu_t)\left(\frac{\partial \overline{u}_i}{\partial x_j} + \frac{\partial \overline{u}_j}{\partial x_i}\right)\right] + S_i \tag{1}$$

Where u is the velocity, p the pressure, ρ the density and ν and ν_t are the viscosity and turbulent eddy-viscosity respectively. The last term are the body forces. Since we are using a tank-fixed coordinate system, source terms in addition to gravity must be accounted for to represent the equations in a non-inertial global system. The motion is harmonic, and the x- and z-terms are given by:

$$\begin{aligned} S_x &= \ddot{\theta}(z - z_m) + \dot{\theta}^2(x - x_m) - gsin\theta, \\ S_z &= -\ddot{\theta}(x - x_m) + \dot{\theta}^2(z - z_m) - 2\dot{\theta}\ \overline{u} - gcos\theta. \end{aligned} \tag{2}$$

where the z-component is the vertical direction and x is in the longitudinal direction of the tank. As the motion is planar, no source term is added for the y-component. θ is the rotational angle. $\dot{\theta}$, $\ddot{\theta}$ is angular velocity and acceleration respectively. The coordinates x_m and z_m are center of the rotational point, and therefore $x - x_m$ is the distance from the rotational point to the center of the tank fixed coordinate system. The second last term of the z-component is the *Coriolis* acceleration.

2.2. Turbulence

Modelling turbulence in sloshing, or general free surface flow with large density ratios, is complex. To calculate the velocities and pressure of Eqn. (1), an expression for the eddy-viscosity is needed. The two-equation, k-ω turbulence model is used to close the set of equations [24]. These are the kinetic turbulent energy and the specific dissipation rate of turbulent energy, ω. The equations can be written [25]:

$$\frac{\partial k}{\partial t} + \overline{u}_j \frac{\partial k}{\partial x_j} = \frac{\partial}{\partial x_j}\left[\left(\nu + \frac{\nu_t}{\sigma_k}\right)\frac{\partial k}{\partial x_j}\right] + P_k - \beta_k k\omega \tag{3}$$

$$\frac{\partial \omega}{\partial t} + \overline{u}_j \frac{\partial \omega}{\partial x_j} = \frac{\partial}{\partial x_j}\left[\left(\nu + \frac{\nu_t}{\sigma_\omega}\right)\frac{\partial \omega}{\partial x_j}\right] + \frac{\omega}{k}\alpha P_k - \beta\omega^2 \tag{4}$$

P_k is the turbulent energy production term. σ_k, σ_ω are standard coefficients in the model, both with values of 2 in this case. β_k, β and α are empirical constants, with values 9/100, 3/40 and 5/9 respectively. The RANS model overproduces the turbulent energy in highly strained flows. This gives unrealistically large values for the eddy-viscosity. Menter [26] noted that the stress intensity ratio scales with the ratio of turbulence production to dissipation. Typical stress intensity ratios can be found from experiments in certain type of flows. In order to avoid overproduction of turbulence in highly strained flow outside the boundary layer, the turbulent eddy-viscosity, ν_t, can be bounded through the limiting formulation [27]:

$$\nu_t = \min\left(\frac{k}{\omega}, \sqrt{\frac{2}{3}}\frac{k}{|\mathbf{S}|}\right) \tag{5}$$

where $|\mathbf{S}|$ is the rate of strain.

The rough wall function by Schlichting [28] is applied to solid boundaries [20]:

$$u^+ = \frac{1}{\kappa} ln\left(\frac{30y}{k_s}\right). \tag{6}$$

u^+ is the dimensionless wall velocity, κ is a constant equal to 0.4 and k_s is the equivalent sand roughness. Near the wall it is assumed that the turbulent production is equal to the dissipation of turbulent energy. This gives the following expression for the specific turbulent dissipation:

$$\omega_{wall} = -\frac{C_\mu^{3/4} k_w^{1/2} u_w^+}{\Delta y_p} \tag{7}$$

where Δy_p is the distance from the wall to the respective cell.

The initial conditions for the velocity field are calculated from potential flow. The turbulence starting values are based on turbulence intensity and viscosity ratio.

At the free surface it seems plausible that the turbulent length scales are reduced. This is a similar effect as on the wall boundaries, where a shear layer is formed due to forces near the surface. The normal fluctuations are damped out, with an amplification of the other components. A boundary condition is proposed to limit the length scale near the free surface [29]:

$$\omega_s = \frac{C_\mu^{-1/4}}{\kappa} k^{1/2} \cdot \frac{1}{y'} \tag{8}$$

where $C_\mu = 0.07$ and $\kappa = 0.4$. y' is the virtual origin of the length scale of the turbulence. In [30] this was determined to be 0.07 times the mean water depth. To activate this boundary condition at the interface of thickness ϵ, the expression is multiplied by the Dirac delta function:

$$\delta(\phi) = \begin{cases} \frac{1}{2\epsilon}\left[1 + \cos\left(\frac{\pi\phi}{\epsilon}\right)\right], & \text{if } |\phi| < \epsilon; \\ 0, & \text{otherwise} \end{cases} \tag{9}$$

where ϕ is the level set function. It should be noted that Eqn. 5, limits the eddy-viscosity in the whole flow domain. The free surface boundary condition of ω in Eqn. 8 increases the dissipation and therefore reduces the eddy-viscosity, but only at the free surface.

2.3. Interface Capturing

The interface between liquid and gas represent a discontinuity in the fluid properties. To capture the interface, the level set technique is used, first presented by [31]. The location of the surface is represented by the zero level of a signed distance function. The following properties are defined:

$$\phi(\mathbf{x}, t) \begin{cases} > 0, & \text{if } \mathbf{x} \in \text{phase 1}; \\ = 0, & \text{if } \mathbf{x} \in \Gamma; \\ < 0, & \text{if } \mathbf{x} \in \text{phase 2} \end{cases} \tag{10}$$

Where Γ represents the free surface. In order to move the interface inside a velocity field, a transport equation for the level set function, ϕ, is solved. The equation is given as:

$$\frac{\partial \phi}{\partial t} + \overline{u}_j \frac{\partial \phi}{\partial x_j} = 0 \tag{11}$$

The convective term in Eq. 11 is discretized with the Hamilton-Jacobi version of the weighted essentially non-oscillatory scheme (WENO HJ). The temporal term is solved with the third-order TVD Runge-Kutta scheme [31]. When the level set function is convected, it will not remain a signed distance function. To maintain this property, it must satisfy the Eikonal equation, $|\nabla \phi| = 1$. Reinitialization at each time step is done using a PDE based equation [32], [33]. Preserving mass conservation poses a challenge when there are significant deformations of the free surface. Some recent advances are found in [34] and [35].

The mixture density in each cell center is evaluated using the smoothed Heaviside function as:

$$\begin{aligned}\rho(\phi) &= \rho_1 H(\phi) + \rho_2 \left[1 - H(\phi)\right] \\ \mu(\phi) &= \mu_1 H(\phi) + \mu_2 \left[1 - H(\phi)\right]\end{aligned} \tag{12}$$

where ρ_1 and ρ_2 are the densities in phase 1 and 2 respectively. The Heaviside function is defined as

$$H\left(\phi_i\right) = \begin{cases} 0, & \text{if } \phi_i < -\epsilon; \\ \frac{1}{2}\left[1 + \frac{\phi_i}{\epsilon} + \frac{1}{\pi} sin\left(\frac{\pi\phi_1}{\epsilon}\right)\right], & \text{if } |\phi_i| < \epsilon; \\ 1, & \text{if } \phi_i > \epsilon \end{cases} \tag{13}$$

Treatment of the abrupt change of fluid properties is needed, and to avoid numerical instabilities, the values are smoothed across the free surface. This can be done by assigning a finite thickness to the interface. Typically the thickness is equal to $\epsilon = 1.6\Delta x$, where Δx is the grid spacing.

Using a staggered grid, the density must also be evaluated at the cell faces to find the fluxes. Performing this in two steps, by interpolation of the densities at the cell center, leads to small scale oscillations. Instead, the cell face densities are calculated in a single step with the smoothed Heaviside function:

$$\rho_{i+1/2} = \rho_1 H(\phi_{i+1/2}) + \rho_2 \left[1 - H(\phi_{i+1/2})\right] \tag{14}$$

where the level set function at the cell faces is evaluated through averaging:

$$\phi_{i+1/2} = \frac{1}{2}\left(\phi_i + \phi_{i+1}\right) \tag{15}$$

2.4. Solution Procedure

Chorin's projection method [36] is used to handle the pressure-velocity coupling. This procedure starts with computing an intermediate velocity field by ignoring the pressure terms in the RANS equations. This is the predictor step. In the next projection step the pressure gradient is added to give the final velocity at the next time step. The continuity condition is used to eliminate $\overline{u}^{n+1}$, to get the Poisson equation:

$$\frac{\partial}{\partial x_i}\left(\frac{1}{\rho}\frac{\partial p}{\partial x_i}\right) = \frac{1}{\Delta t}\frac{\partial \overline{u}_i^*}{\partial x_i} \tag{16}$$

The equation is iteratively solved to find the pressure at the new time step. Integration of Parallel High Performance Preconditioners (HYPRE) with REEF3D makes it possible to combine a conjugate gradient solver with geometric multigrid preconditioning [37].

The convective terms in the RANS equation are discretized using the conservative fifth-order WENO scheme [38]. A non-conservative WENO scheme (WENO HJ) is used to discretize the convective terms in the level set equation, the k and ω equations. Essentially non-oscillatory schemes (ENO) bring higher order to the first order upwind schemes by polynomial interpolation of the flux functions. There are three possible HJ ENO approximations to the fluxes. WENO uses a weight parameter and combines the three stencils.

The grid is uniform and orthogonal. Construction of this is done quite easily in the rectangular domain. The ghost cell method [39] is implemented to account for solid boundaries.

3. Experimental set-up and results

The experiments were carried out at the Department of Maritime Technology and Operations at NTNU Ålesund. A solid rotational platform is used to excite sloshing. A crank mechanism driven by an electro motor creates the rotational motion of a plane table. Two different tanks have been used, the smallest one to test $h/L = 0.125$, because it required depths that would result in tank-roof impacts with the longest tank. The main dimensions are given in Table 1. An explanation of the dimensions is given in Fig.1. Validation results are performed by placing the sensor slightly to the left in Fig. 1, while the free-surface amplitude

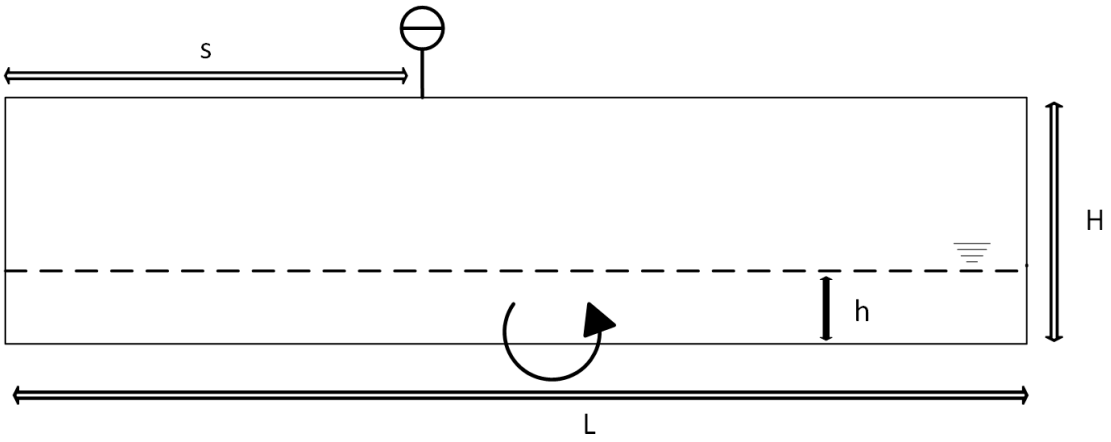

Figure 1: Tank configuration.

Table 1: Tank configurations.

Tank config.	L $[m]$	B $[m]$	H $[m]$	s/L	Test type
1	1.00	0.25	0.40	0.408	Main test
2	0.59	0.18	0.3	0.408	Comparison and $h/L = 0.125$

from experiments is measured also at the middle of the tank, $x/L = 0.500$. Several fillings are also tested with the small tank to compare the results with the long tank. This can be done by scaling the frequencies based on the tank lengths, so that $f_2 = f_1 \cdot \sqrt{L_1/L_2}$, where L_1 and f_1 is the length and frequency of the long tank respectively.

The roll axis is at the intersection of the bottom and the centerplane of the tank, creating liquid motions in the longitudinal direction (Fig. 1). Videos of all the sloshing tests are recorded, using a GoPro Hero4 camera. The distance from the tank top to the free surface is measured using an ultrasonic sensor, type Sick UM12. The resolution of the sensor is 0.069 mm. The accuracy is ±1 % with a repeatability of ±0.15 % based on the current measurement value. If it is assumed that the percentage accuracy is valid also for a measured distance of 100 mm, the potential error would be 1 mm. The operating range of the sensor is 20 to 150 mm. The location of the sensor is close to the middle of the tank, with a distance of $s/L = 408$ from the left side.

The varied test parameters are the frequency of motion and the filling level. The roll amplitude is kept equal to 3 degrees in all tests. The tank breadth is small relative to the length, so that 3D effects are negligible. This is also seen from the 3D simulation results. The test parameters are given in Table 2. The test runs for each filling are performed continuously by adjusting frequency at small steps after several cycles with each frequency.

3.1. Wave amplitude and the bifurcation point

The free-surface elevation for a range of frequencies and fillings is found from measurements in the tank test. The sensor location is close to the middle, and as already shown, the amplitude is slightly different when passing each way. As the wave starts to travel all the way without breaking from wall to wall, the amplitude is almost similar, and the dominating frequency is $2{\cdot}f$. To identify the amplitude-frequency curve of each filling, it would make sense to calculate the average of the two amplitudes of each pass (right to left and left to right). The free-surface elevation is therefore calculated as the mean value of the positive peaks, being the wave passing from left to right and opposite:

$$\overline{\eta} = \frac{1}{N}\sum_{i=1}^{N}\eta_i \tag{17}$$

Table 2: Test parameters, minimum and maximum frequencies of each filling.

Test no.	h/L	f $[Hz]$	$f/f_{1,0}$	Tank config.
1	0.030	0.233-0.483	0.861-1.785	1
2	0.040	0.300-0.500	0.960-1.601	1
3	0.050	0.300-0.533	0.860-1.529	1/2
4	0.060	0.300-0.600	0.787-1.573	1
5	0.070	0.333-0.633	0.811-1.541	1/2
6	0.080	0.300-0.633	0.684-1.445	1
7	0.090	0.333-0.617	0.719-1.330	1
8	0.100	0.367-0.627	0.752-1.287	1/2
9	0.125	0.500-0.633	0.926-1.173	2

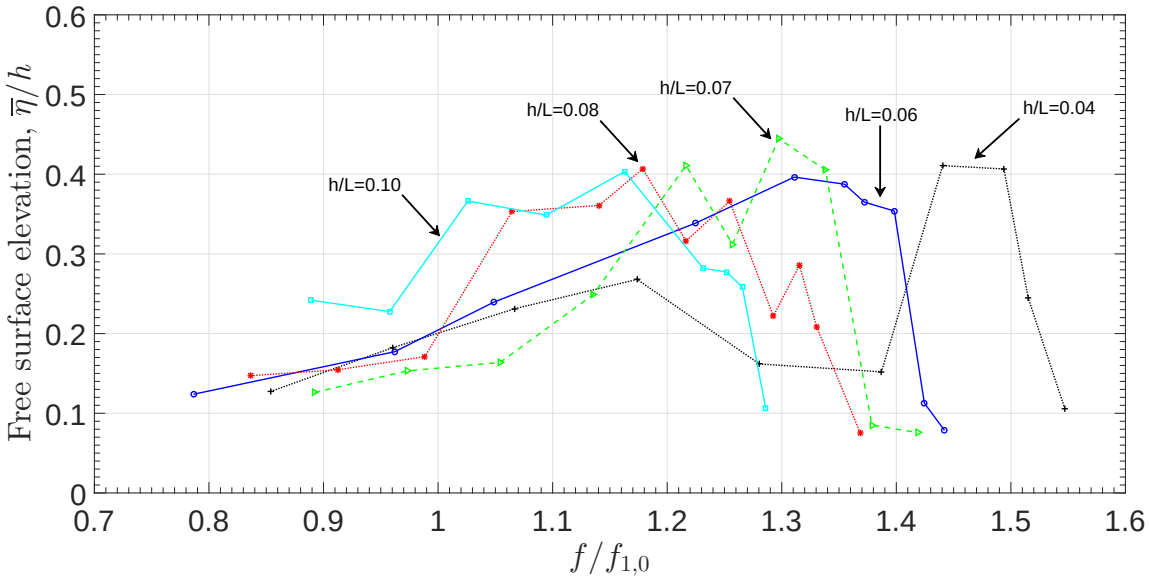

Figure 2: Wave amplitude.

where N is the total number of positive peaks within the time series and η_i is wave peak number i of each passing. The resulting wave amplitude for a selection of fillings is shown in Fig. 2.

To find the repeatability of the measured peaks within each test of constant motion frequency, the standard deviation is found for each of the wave peaks, defined as

$$S = \sqrt{\frac{1}{N-1}\sum_{i=1}^{N}|\eta_i - \overline{\eta}|}. \tag{18}$$

It is found that the standard deviation could be as high as 15 % of the respective wave elevation, but on average it is 10 %. The number of sloshing cycles is 30 for each frequency. This means that the repeatability of the amplitude within a test of several sloshing cycles is relatively low. The absolute values should therefore be considered with care, but the curves in Fig. 2 show interesting trends. There seems to be a marked difference between the depth $h/L = 0.07$ and $h/L = 0.08$, as the wave amplitudes at $h/L = 0.08$ are more significant for a broader range of frequencies. The sections below show how the filling affects the speed of the wave, breaking or non-breaking, as it approaches the side wall. The dissipation is quite different between the different fillings. The rapid increase seen for $h/L = 0.08$ close to $f/f_{1,0} = 1$ is because the wave breaks close to the middle or slightly across it.

At a certain frequency parameter, $f/f_{1,0}$, the wave amplitude drops significantly. The frequency when this occurs is higher for smaller fillings. The zone where impacts are more severe is also narrower for smaller depths. Through observation it is found which frequencies result in the characteristic solitary wave followed

by the *bifurcation* point. In a practical sense, the definition is such that a small change in $f/f_{1,0}$ causes a sudden topological change in the long-term dynamic behaviour of the system [4]. This point is accurately determined by gradually varying the frequencies, and observing at which frequency it occurs.

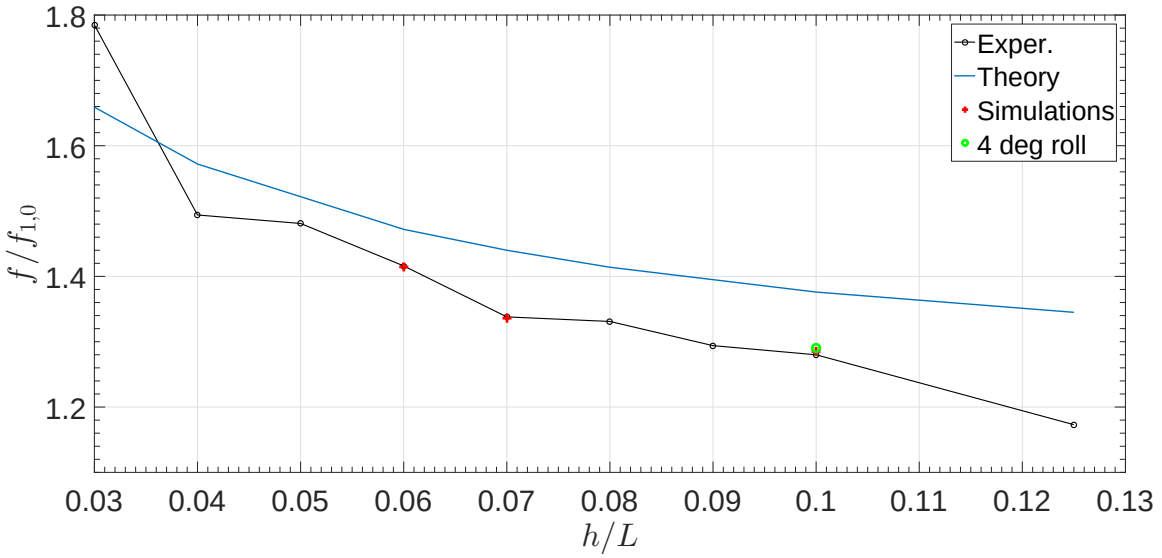

Figure 3: The bifurcation frequency (experiments and simulations) and the theoretical prediction of the upper range of hydraulic jumps to occur.

The bifurcation frequency for all the tested fillings is presented in Fig. 3. It has been determined for a few fillings at 3 degree roll using simulations. 4 degree roll amplitude has also been determined with REEF3D only at filling $h/L = 0.10$. The bifurcation parameter $f/f_{1,0}$ is slightly higher with 4 degree roll. Several more amplitude and filling combinations should be investigated for the future. This may be done with our numerical tool.

The curve is steeper for low fillings, and flattens out as the filling level passes $h/L = 0.06$. The flat curve at high fillings indicates that the sloshing enters the intermediate depth region. Comparison with the smaller tank (number 2) resulted in the same parameter $f/f_{1,0}$ with the tested fillings and scaled frequencies. In the same figure, the upper range of hydraulic jumps to occur according to the theory by Verhagen and Van Wijngaarden [40] is shown. The formula is given in Eq. 19. It should be noted that the theoretical prediction is not a prediction of the bifurcation point. But as it predicts a higher frequency parameter for $h/L > 0.04$, the guidance is poor. Using the theoretical prediction in the upper range will therefore result in a too wide range for resonant conditions to be present.

$$|1 - f/f_{1,0}| \leq \pi^{-2}\sqrt{24}\sqrt{L\eta_{4a}/h + \pi^2 Z_r \eta_{4a}/L} \tag{19}$$

4. Numerical investigation of shallow-depth sloshing

4.1. Grid sensitivity study

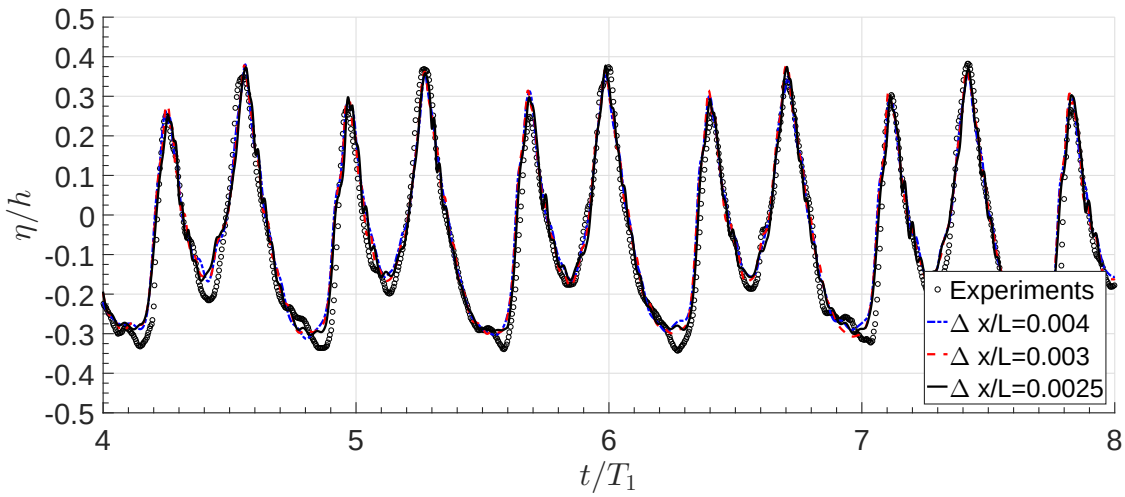

Figure 4: Grid sensitivity for case $h/L = 0.06$ and $f/f_{1,0} = 1.40$.

In this section, the simulation and experiment results are compared and discussed. A grid sensitivity study is presented at first, followed by the comparison between experiments and simulations for some selected cases. The numerical set-up is meant to closely represent the experimental test. A rectangular domain with orthogonal and uniform cells is constructed. The rotation point similar to Fig. 1 is chosen, and motion is generated through the momentum source terms, as described in Eq. 2. Three different cell sizes are compared for test number 4 with $h/L = 0.06$ and the frequency corresponding to the bifurcation point ($f/f_{1,0} = 1.40$). Only two-dimensional simulations are compared. The resulting free-surface elevation is shown in Fig. 4. It is found that the highest peak is slightly lower with finer grid where the amplitude is slightly over-predicted by the RANS simulations. As the simulation with grid $\Delta x/L = \Delta y/L$=0.003 is significantly more efficient than the finest grid, it is therefore chosen for further studies. The number of grid cells is equal to 33300 in the two-dimensional case.

4.2. Comparison of free-surface elevation

The comparison between experiments and simulations is based on the measured free-surface elevation. The results from tests with water elevation $h/L = 0.06$ are plotted in Fig. 5a - 5d respectively. The simulated amplitude of the wave travelling back and forth is in close agreement with the experiments. Any discrepancy is due to ripples at the back of the wave and a free-surface profile at the wave front. It was observed during experiments that the wave front is chaotic as it breaks. The sensor is placed somewhat to the left of the middle. In Fig. 5c, it can be seen that the two peaks have almost the same amplitude. This is because the amplitude of the travelling wave only differs slightly when passing each direction. This indicates that this is almost a single solitary wave just prior to the bifurcation point.

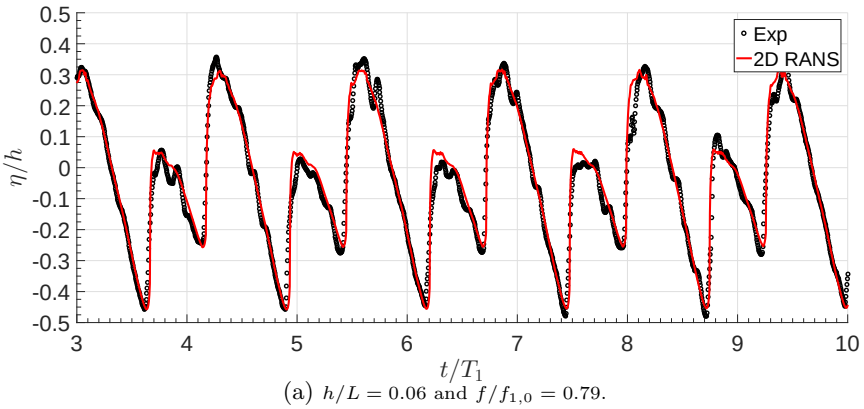

(a) $h/L = 0.06$ and $f/f_{1,0} = 0.79$.

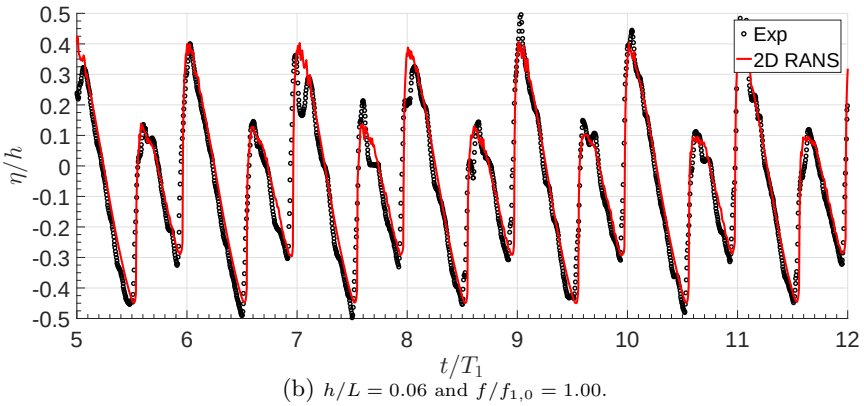

(b) $h/L = 0.06$ and $f/f_{1,0} = 1.00$.

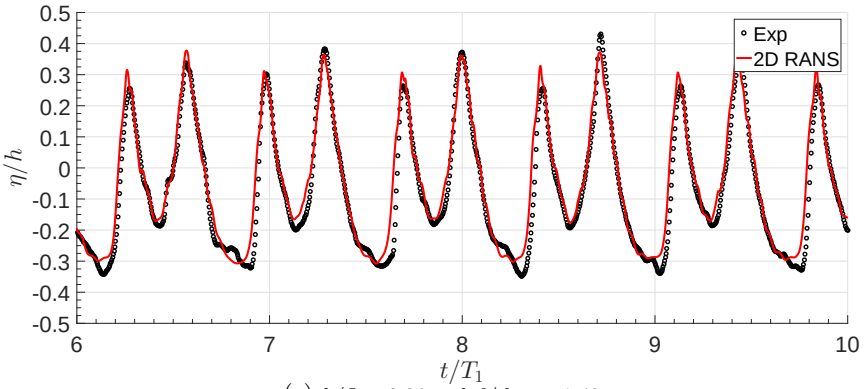

(c) $h/L = 0.06$ and $f/f_{1,0} = 1.40$.

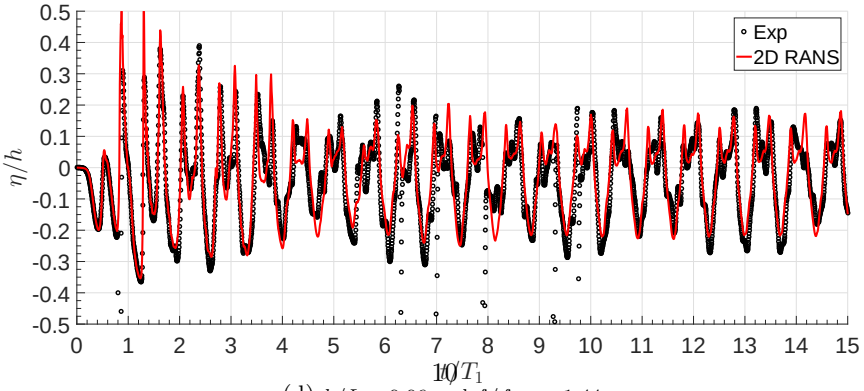

(d) $h/L = 0.06$ and $f/f_{1,0} = 1.44$.

Figure 5: Free-surface elevation at forced sloshing.

4.3. Simulations of free sloshing

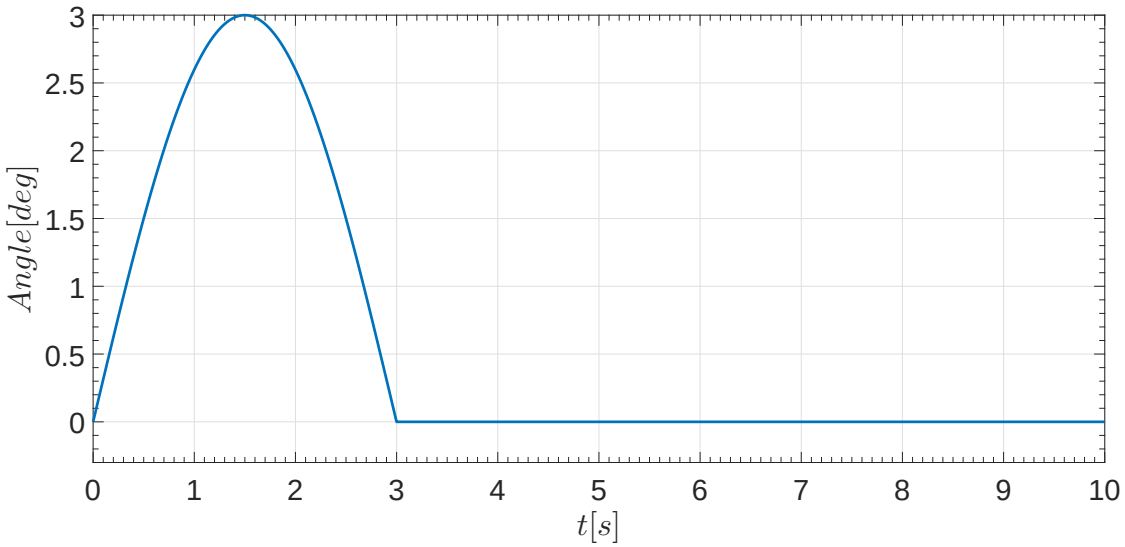

Figure 6: Motion transient of half a period in the free sloshing case.

Free sloshing is investigated by turning off the motion after half a cycle with a frequency of $f/f_{1,0} = 0.437$. Time history of the motion amplitude is shown in in Fig. 6. The long tank is used to perform these tests (configuration 1). Repeatability of such tests are not so good due to the low damping. No steady state exists and the sloshing is highly transient. The more damping the better should the repeatability be, as the damping act as a constraint to the motion. However, this is only true if details in the flow are excluded, like the chaotic wave front.

The reason for running free sloshing tests, as mentioned in [7], is to evaluate the ability of the model to predict the wave speed and shape. Sloshing with zero tank excitation results in natural sloshing modes. Our aim is to compare the frequencies from simulations with those that are calculated, as well as performing a sensitivity analysis on the turbulence settings. This is relevant because it is found that two-equation RANS turbulence models over-predicts the eddy viscosity at the free surface. The resulting free-surface elevation is given in Fig. 7. Some slight discrepancy in the free-surface amplitude is found before $t/T_1 = 20$. In the beginning, after $t/T_1 = 4$, the decay predicted by RANS is greater. Some signal noise is present at around $t/T_1 = 4$.

The wave profile at different time instants is shown in Fig. 8. Fig. 8b shows the wave when the motion stops. The travelling wave is small, but has some steepness in the beginning of the travel towards the right wall. The returning wave system is shown in Fig. 8d. At this time instant, the first of the three waves is registered by the ultrasonic sensor, while the following waves are seen towards the right. The wave with the maximum amplitude, in Fig. 8f, results from interaction between the three waves (Fig. 8d) and occurs when the first of the three waves return to meet the two last waves.

Most of the simulations in this study are performed in two dimensions. To investigate the influence of wall shear on the damping, simulations in three dimensions are compared to the two-dimensional case. Fig. 9 shows a time series of 3D simulations performed at the Notur supercomputers. The grid cell number is equal to 1.6 million with the same Δx as in the 2D case. The difference between 2D and 3D is minor, which indicates that the damping due to wall shear is insignificant.

The free-surface boundary condition of ω can be investigated by adjusting the y' value in Eq. 8. The default value in REEF3D is 0.07. A reduction of this value increases the specific turbulent dissipation resulting in a decrease of the eddy viscosity. This is only activated at the free surface. From Fig. 10 the

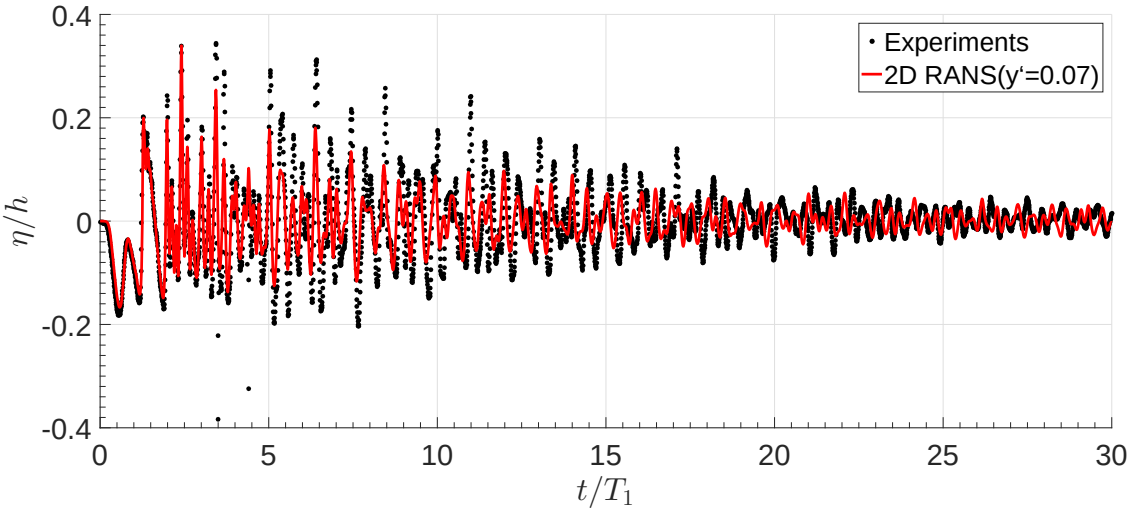

Figure 7: Free sloshing results. Half a period of $f/f_{1,0} = 0.437$ at $h/L = 0.06$.

results clearly show that the lower value of y' results in increased amplitude. The wave amplitude is sensitive to the turbulence settings at the free surface. This is questionable because the fluid motion is expected to be laminar due to the low initial motion.

The free-surface profile at the time the maximum wave is measured is shown comparing the two turbulence settings in Fig. 11 . The reduced eddy viscosity increases the crest and reduces the trough. The difference in the wave amplitude measured at this time instant is found to be approximately 0.3 [mm], so the difference is minor.

The vorticity at the same instant of time is plotted in Fig. 12. It indicates that viscous effects are important, and fluid properties are set into rotation by an unbalanced shear stress [41]. Providing the vorticity offers a method to separate the flow into viscous and inviscid effects. Specific dissipation of turbulent energy is shown in Fig. 13. The dissipation dominates closest to the interface. The results are kind of paradoxical. When the dissipation is expected to be minor, the turbulence settings at the free surface will matter. But when the dissipation is large, like in forced sloshing close to resonance, these settings is of minor importance. It is a result from the abrupt change in fluid properties across the interface. The results does not have any particular consequence. The difference is seen only in the laminar case when the damping is small in general. That is why the results show some sensitivity.

The spectrogram plot in Fig. 14 shows short-time Fourier transformation (SFFT) of the experimental data. Fast Fourier transformation is performed in specified sections, or time windows. The signal is divided into 18 equal sections. This corresponds to a time interval of 6 [s] which equals the initial motion period. It can be seen that no distinct frequency dominates before approximately $t/T_1 = 8$. Here, the first symmetric mode is seen, $f/f_{1,0} \approx 2$ as well as the second asymmetric mode, $f/f_{1,0} \approx 3$. An FFT-analysis is performed between $t/T_1 = 10$ and $t/T_1 = 20$ including experiments and simulation results with the two different values of y' (Fig. 15). The lower spectral value shows the underestimated wave amplitude from simulations. It is also seen that the lower value of y' is closer to the experiments. It is interesting to observe that although the natural frequencies are predicted quite well by the simulations, there is an increasing shift. This is not visible at $f/f_{1,0} = 2$, but more pronounced at $f/f_{1,0} = 3$.

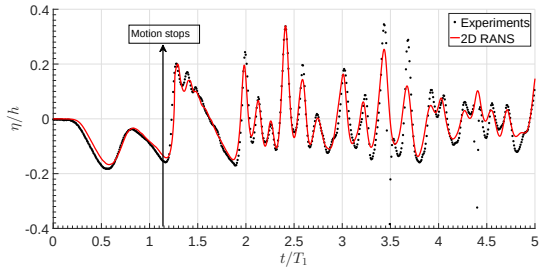

(a) Wave amplitude at motion stop.

(b) Simulated wave profile at motion stop.

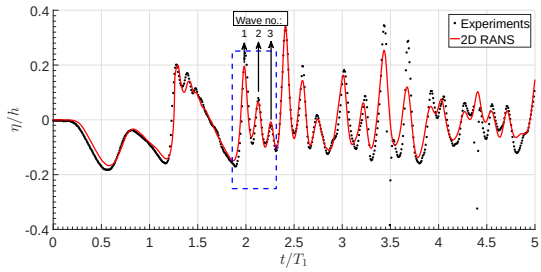

(c) Wave amplitude of 3 travelling waves.

(d) Wave profiles from simulations.

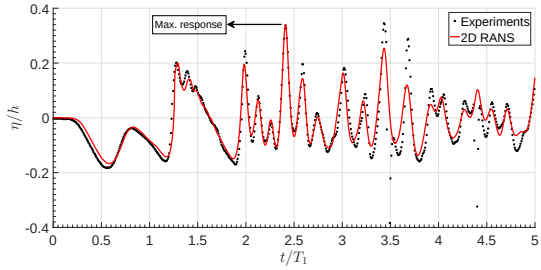

(e) Maximum wave amplitude.

(f) Wave profile at maximum response.

Figure 8: Simulated wave profile at selected times. Sensor position is marked between the dark and light contours on the figure.

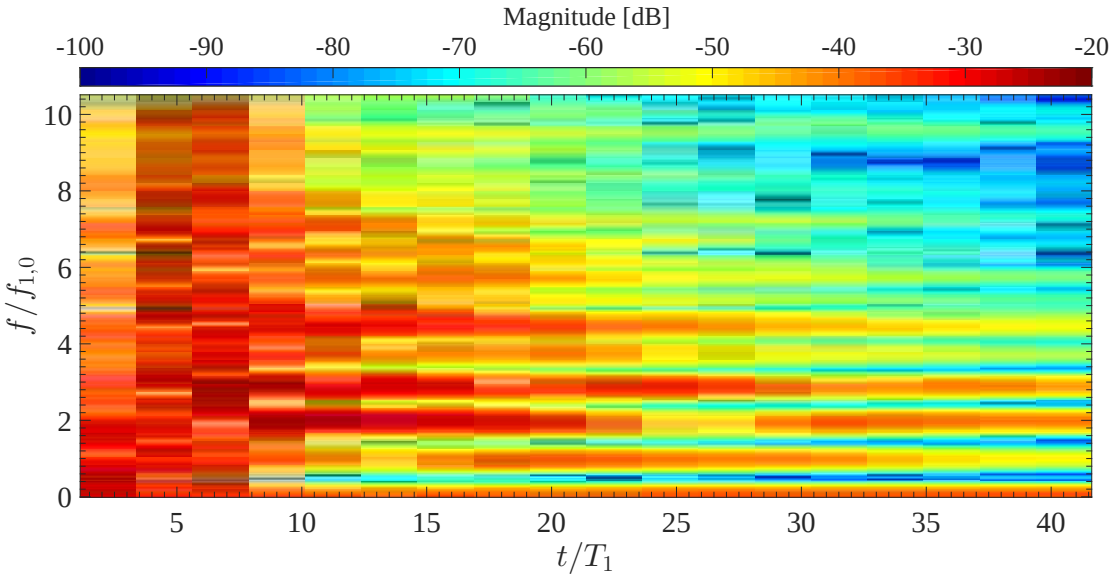

Figure 14: Spectrogram representing experimental data. Running half a period before stop ($h/L = 0.06$ and $f/f_{1,0} = 0.437$).

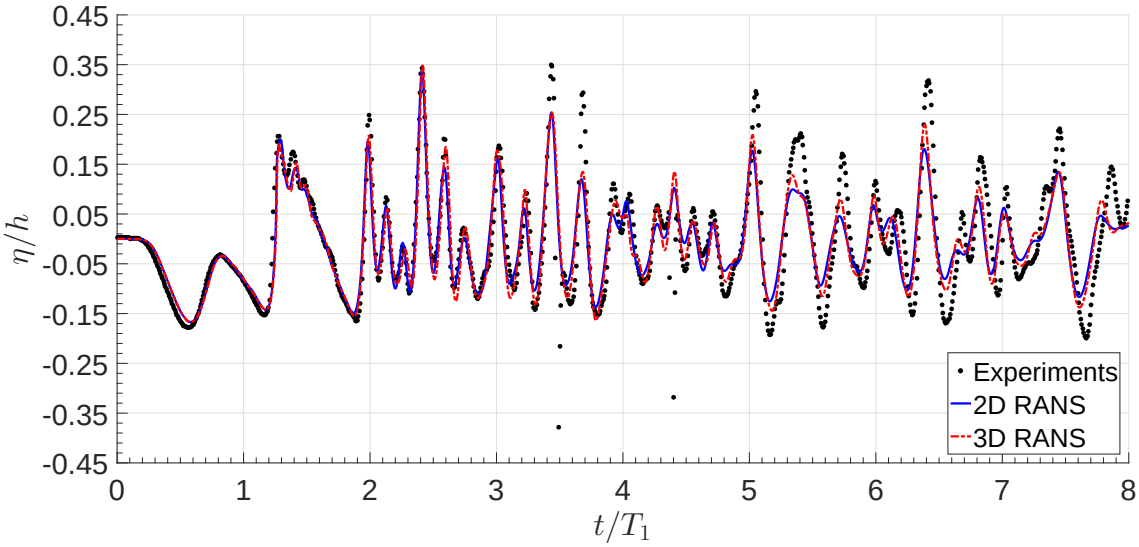

Figure 9: Comparison of 2D and 3D running half a period before stop ($h/L = 0.06$ and $f/f_{1,0} = 0.437$).

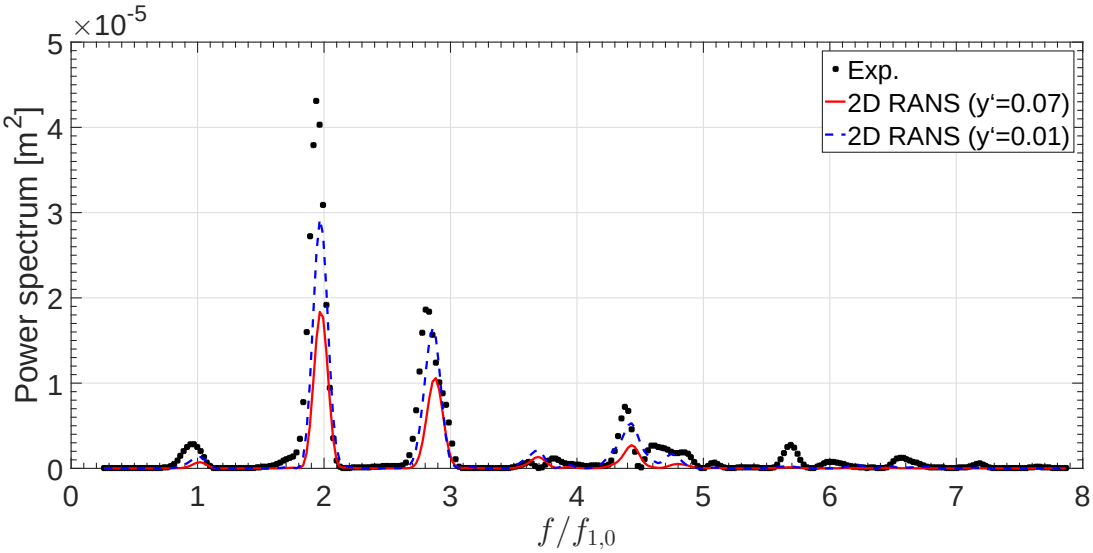

Figure 15: FFT of the time window between $t/T_1 = 10$ and $t/T_1 = 20$. The largest peaks correspond to the natural frequencies, $f_{2,0}$ and $f_{3,0}$.

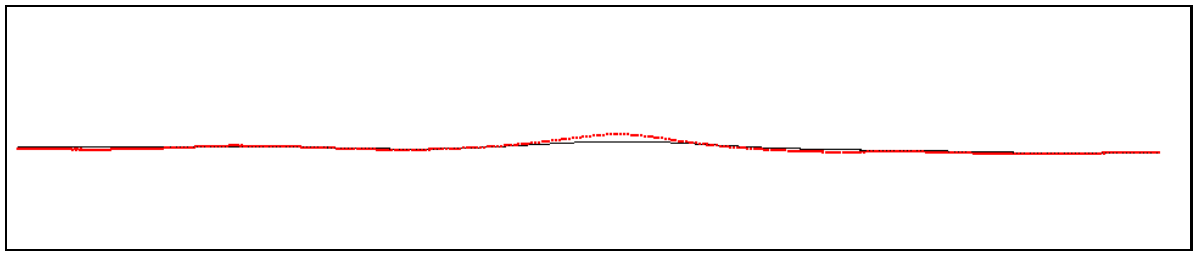

Figure 16: Comparison of the wave profile for different turbulence settings. 2nd mode standing wave at $t/T_1 = 8.33$. The red dotted line represent the lower value of y'.

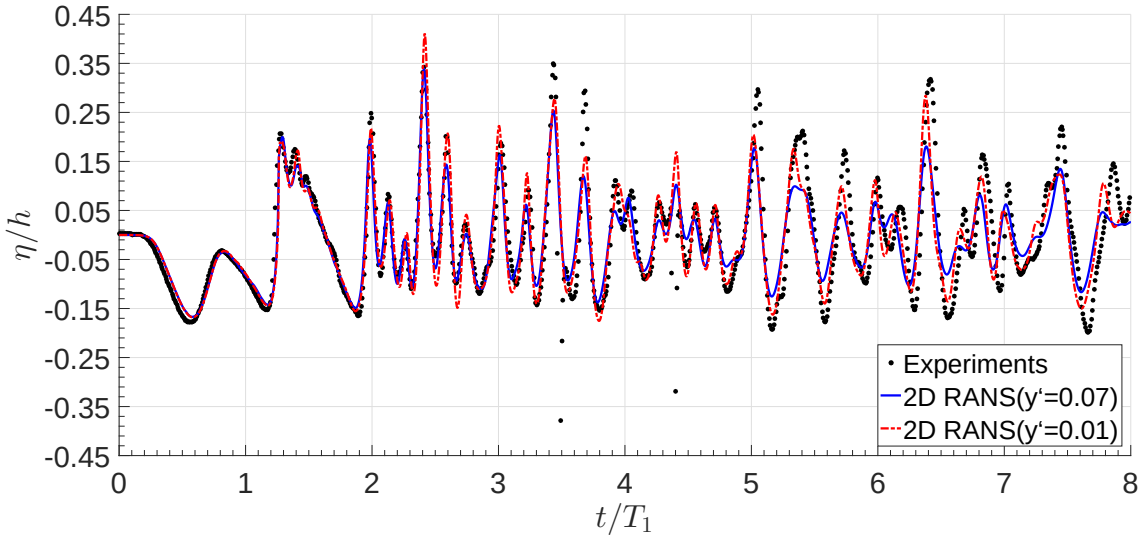

Figure 10: Comparison of turbulence settings (Eq. 8).

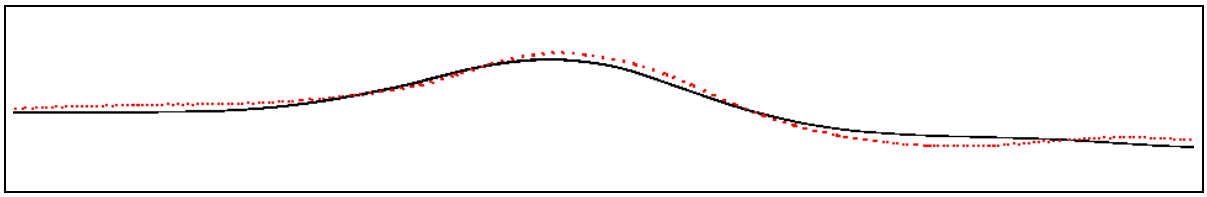

Figure 11: Comparison of the wave profile for different turbulence settings. The red dotted line represent the lower value of y'. (The border does not represent the tank walls, and the free surface is blown up to see the differences).

Not only the amplitude is affected by the damping, but the wave speed as well.

4.4. Up- and downstream advancing waves

The chosen excitation frequencies are in proximity to the first fundamental frequency or higher. The results suggest that the characteristic patterns described by Olsen and Johnsen [5] require further investigation. The difference seems to depend on the platform angle, which is particularly important for roll motion, as well as the tank filling. Observation reveals that the wave behaves quite differently depending on whether it is advancing up- or downstream. This is illustrated below in Fig. 17a - 17h. In the case of an upstream advancing wave, the breaking of the wave occurs almost immediately after returning from the side wall. While in the downstream case, the resulting wave has larger amplitudes before it eventually breaks as seen from Fig. 17e and Fig. 17g. If the angle of the tank is closer to zero when the wave returns, the wave gains more momentum due to gravitational forces travelling downstream after leaving the wall. As can be seen in Fig. 17b, the velocity of the lower liquid layer travels in an opposite direction to the wave. The wave may be characterized as a bore [6], and dissipates by travelling on top of the lower layer of liquid. Observation indicates that the largest difference between the two regimes depends on whether the wave breaks at a positive or negative tank motion angle. In this case, positive is defined for when the wave is advancing downstream. The wave in Fig. 17e - Fig. 17h is more of a spilling breaker type, and no plunging breakers are observed in the experiments. The impact force from the bore depends on how much the wave is dissipated before it reaches the wall.

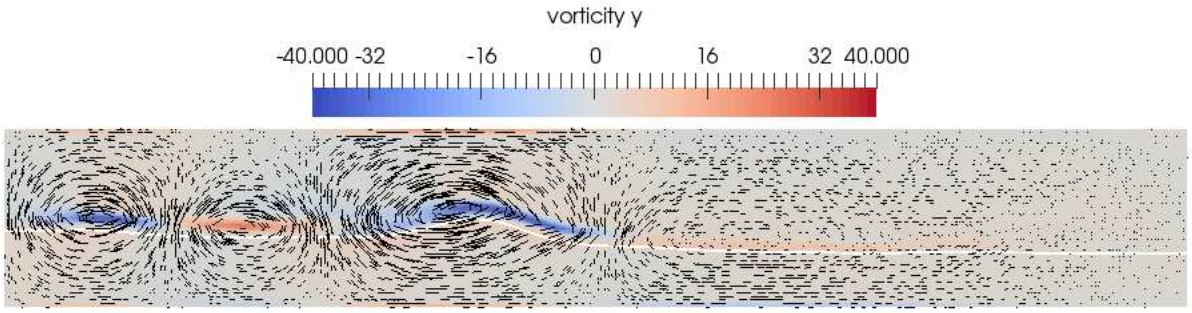

Figure 12: Vorticity at the time of maximum response during the free sloshing test.

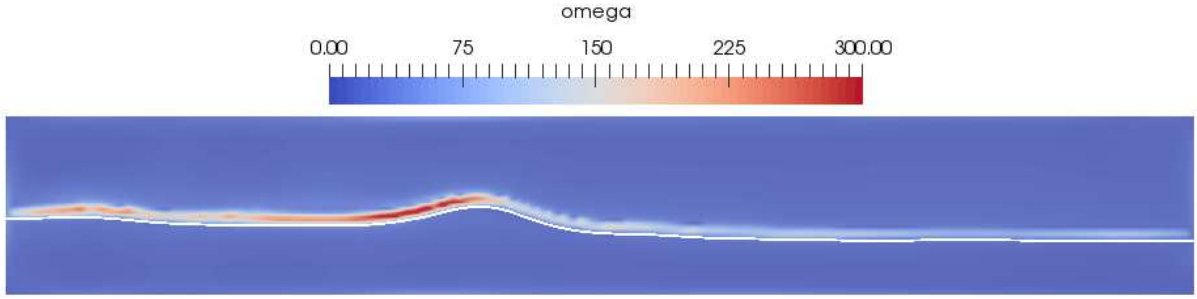

Figure 13: Specific dissipation of turbulence energy (ω) at the time of maximum response during the free sloshing test.

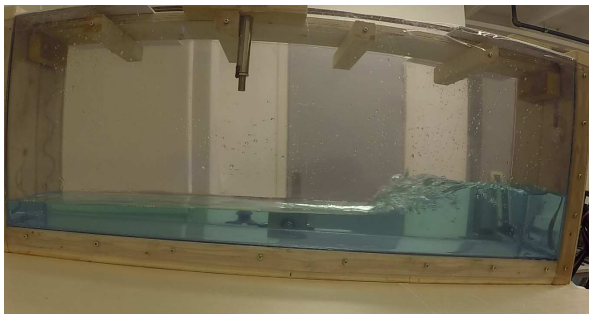

(a) Wave advancing upstream.
($h/L = 0.07$ and $f/f_{1,0} = 0.892$).

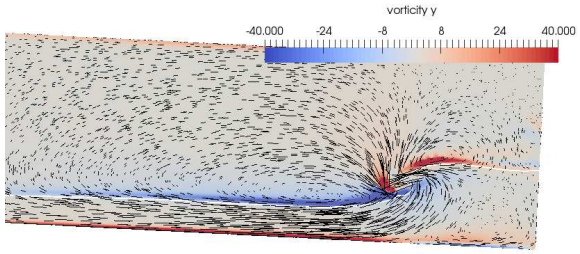

(b) Simulation of Fig. 17a.
($h/L = 0.07$ and $f/f_{1,0} = 0.892$).

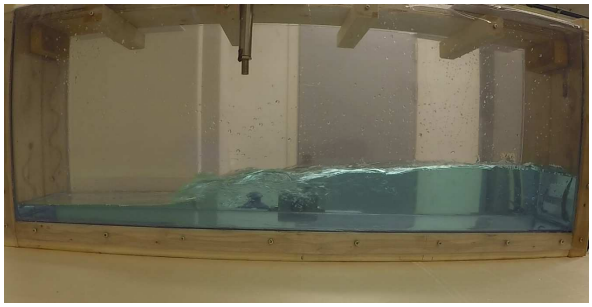

(c) Wave dissipating upstream.
($h/L = 0.07$ and $f/f_{1,0} = 0.892$).

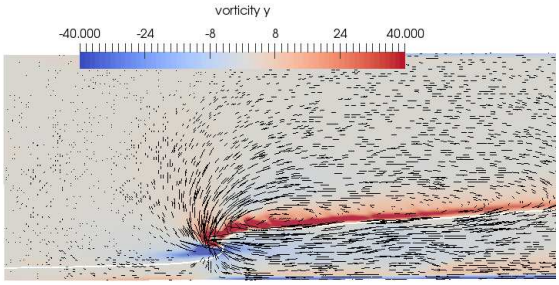

(d) Simulation of Fig. 17c.
($h/L = 0.07$ and $f/f_{1,0} = 0.892$).

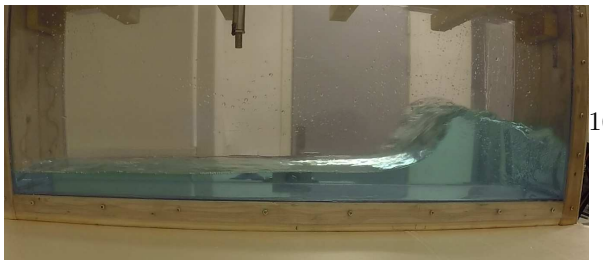

(e) Wave advancing downstream.
($h/L = 0.07$ and $f/f_{1,0} = 1.135$).

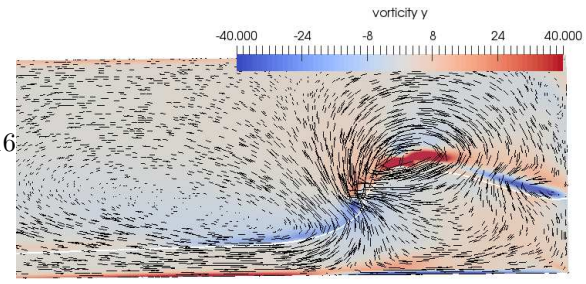

(f) Simulation of Fig. 17e.
($h/L = 0.07$ and $f/f_{1,0} = 1.135$).

4.5. Breaking characteristics of waves advancing downstream

In the previous section, different wave characteristics have been observed. The most significant impact occurs when a solitary wave travels along the whole tank length without breaking. All of the dissipation takes place in a very short time interval when it hits the wall. It is reasonable to assume that the impact force depends on the location of the breaking. If the wave breaks further away from the wall, more kinetic energy has been dissipated before it hits the wall. During the experiments, it is observed that even waves that break close to the middle can have significant kinetic energy when reaching the wall, and the energy increases with increasing liquid depth.

Fig. 19a and Fig. 19b show the waves when the tank is horizontal. Two different fillings are investigated. The same excitation frequency is used, which is $f = 0.4667\ [Hz]$. It can be seen that for $h/L = 0.08$, the wave is already overturning. The resulting difference is that the wave front drops with larger vertical velocity towards the liquid surface compared to $h/L = 0.07$. With $h/L = 0.07$ the gravitational component is larger in the longitudinal tank direction. The impact on the surface creates a bounce back and the motion is violent as shown in Fig. 18. Fig. 19e and Fig. 19f show the simulations at the time instants just after the impact.

Figure 18: Bounce back after impacting the surface. $h/L = 0.08$ and $f/f_{1,0} = 1.065$.

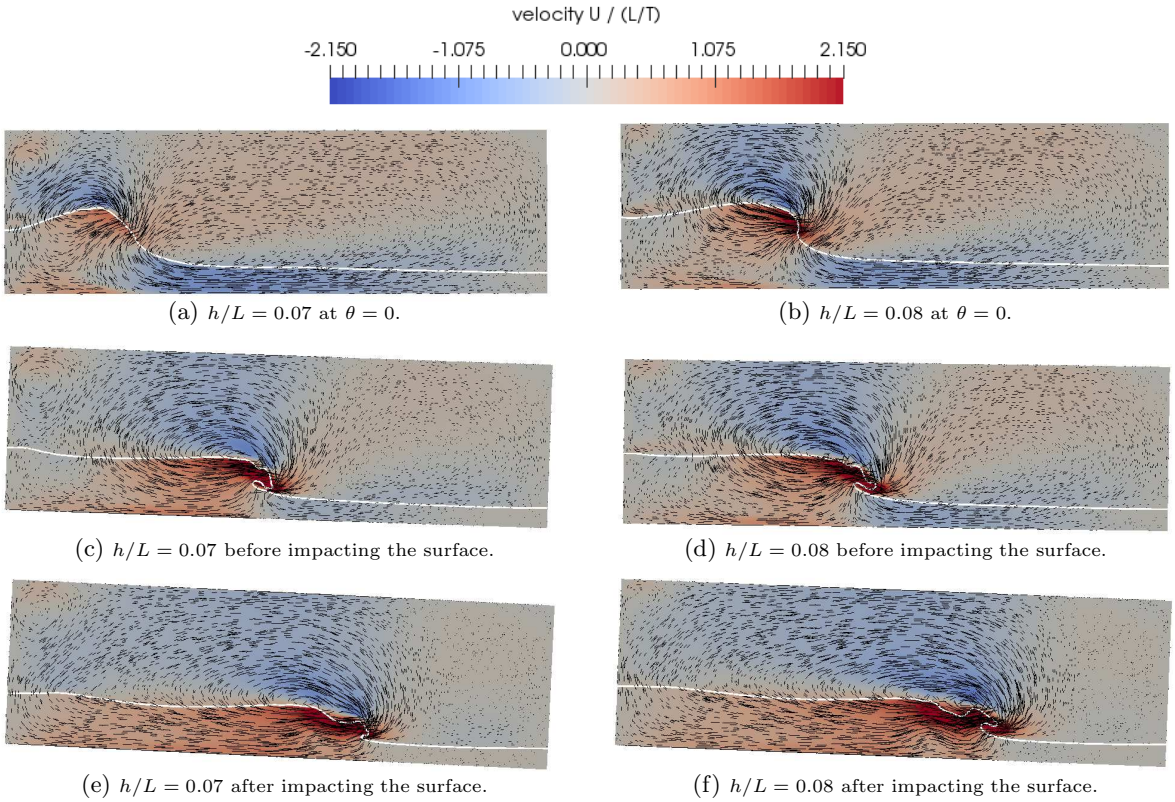

(a) $h/L = 0.07$ at $\theta = 0$.

(b) $h/L = 0.08$ at $\theta = 0$.

(c) $h/L = 0.07$ before impacting the surface.

(d) $h/L = 0.08$ before impacting the surface.

(e) $h/L = 0.07$ after impacting the surface.

(f) $h/L = 0.08$ after impacting the surface.

Figure 19: Wave breaking with different mean depths. $h/L = 0.07$ / $f/f_{1,0} = 1.135$ and $h/L = 0.08$ / $f/f_{1,0} = 1.065$.

4.6. Wave impacts close to the bifurcation point

A slight variation of the frequency below the observed bifurcation point shows different characteristics of the wave front just before impacting the wall. Fig. 20a - 20f shows video captures and corresponding simulations of the wave just before it hits the wall. The frequencies are at the bifurcation point in Fig. 20e and slightly below in Fig. 20a and 20c. In the case with the lowest frequency the wave breaks before the wall, but does not have time to dissipate before it impacts the wall. In Fig. 20c, the wave also starts to break, but even closer to the wall. This causes a more severe impact. At the bifurcation point, the wave does not break before it hits the wall.

From the figures, it can be observed that the platform angle is close to zero just before the wave hits the wall in Fig. 20e. The speed of the wave and momentum of the lower layer of liquid is balanced correctly with the platform angle to make the wave travel all of the tank length.

(a) $h/L = 0.07$ and $f/f_{1,0} = 1.257$.

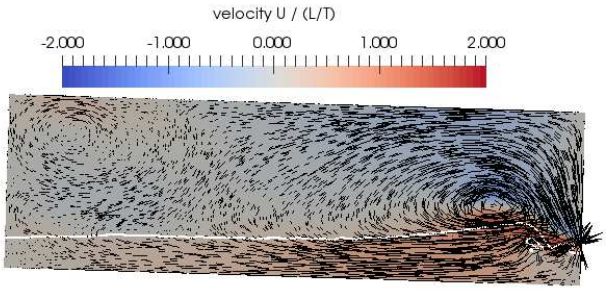

(b) Simulations of Fig. 20a.

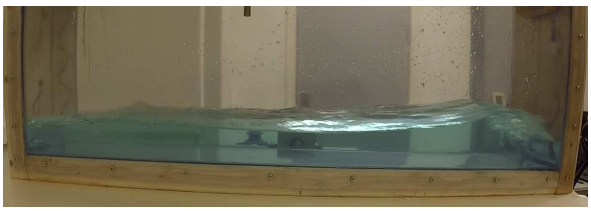

(c) $h/L = 0.07$ and $f/f_{1,0} = 1.297$.

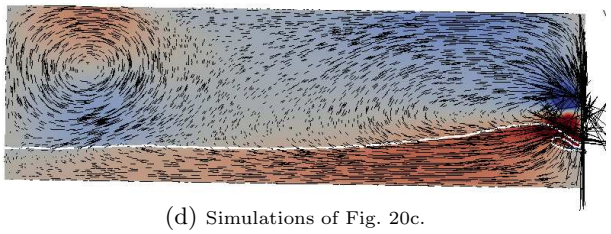

(d) Simulations of Fig. 20c.

(e) $h/L = 0.07$ and $f/f_{1,0} = 1.338$.

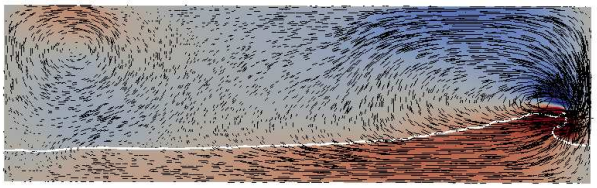

(f) Simulations of Fig. 20e.

Figure 20: Frequencies slightly below and at the bifurcation point.

5. Conclusion

Sloshing at shallow depths results in steep waves that may potentially cause damages to structures due to severe impact at the walls. Understanding the wave patterns for a range of fillings and frequencies is important to remedy this.

Studies of sloshing in a rectangular tank with shallow depths were conducted at the lab facility at NTNU in Ålesund. A range of fillings between $h/L = 0.03$ to $h/L = 0.125$ were tested with several frequencies in proximity to the first mode natural frequency and ranging past the bifurcation point. RANS simulations of sloshing have been performed using the open-source finite difference CFD solver REEF3D. Comparisons are made between experiments and RANS for a selection of fillings and frequencies. Through the coherent approach of combining experiments and validated numerical simulations, the study extends the state-of-the art research through the description of additional wave pattern characteristics. The following conclusions can be made:

- The mean wave amplitude is measured for a range of fillings and frequencies. The wave breaks closer to the middle of the tank for the larger fillings. The resonance zone moves to higher frequencies for the lower depths.
- The bifurcation point is determined for a range of fillings between $h/L = 0.03$ and $h/L = 0.125$. It occurs at $f/f_{1,0}$ larger than unity for the lower fillings, while it approaches unity for fillings above $h/L = 0.1$.
- The theory from Verhagen and Van Wijngaarden [40] predicts a too high upper limit for hydraulic jumps to occur. Thus, it provides poor guidance for when the harmful wave impact occurs in the upper frequency range.
- The open-source CFD tool REEF3D predicts the sloshing waves with good accuracy. The largest deviation occurs when there are many waves present in the tank with severe oscillations, like above the bifurcation point and with free sloshing.
- Comparison of the free-surface elevation with free sloshing indicates that the damping of the wave is sensitive to the turbulence model settings at the free surface and less sensitive to the wall shear.
- The wave characteristics and dissipation mechanisms depend on whether the waves advance up- or downstream in the tank. This is relevant for sloshing under a roll motion.

Acknowledgement

The authors would like to thank the staff at the Department of Maritime Technology and Operations for providing lab facilities and materials necessary for performing the experiments. Thanks also to the other members of the REEF3D team for their support. This study is a part of a PhD project funded by NTNU in Ålesund.

6. Appendix

An example of input files for REEF3D is given below. The first text file, 'control.txt' sets the meshing and boundary conditions. The second file, 'ctrl.txt' is to set the simulation parameters. Explanation to the relevant settings is given behind each line starting with '//'. The reader is also referred to the REEF3D manual [20].

'control.txt':

```
C 11 21 //Wall boundary
C 12 3 //Symmetry boundary
C 13 3
C 14 21
C 15 21
C 16 21
B 1 0.003 //Grid cell size [m]
B 10 0.0 1.0 0.0 0.003 0.0 0.3 //B 10 Provide the size of domain in x-, y and z-dir. [m]
M 10 4 //No. of processors for parallel computations
```

'ctrl.txt':
B 5 1
B 10 1
B 11 1
B 50 0.0001 //Surface roughness
B 192 -3.0 0.16667 0.5 0.0 //B192 provide angle amplitude [deg], frequency [Hz] and point of rotation (x,y) [m]
B 194 0.0 3.0 //Time to start and stop motion [s]
D 10 4
D 20 2
D 30 1
F 30 3
F 40 3
F 46 2
F 50 4
F 60 0.06 //Free surface position
I 12 1
N 40 3
N 41 100.0 //Total simulation time
N 47 0.1
M 10 4 //No. of processors, here 4
P 10 1
P 30 0.05 //Time of printing VTU-files [s]
P 40 1
P 41 1
P 54 10
P 51 0.408 0.125 //Position of wave sensor
P 51 0.1 0.125 //Position of sensor no. 2
P 51 0.5 0.125 //Position of sensor no. 3
P 75 1
P 101 1
T 10 2
T 36 1 //Free-surface turbulence limitation ON
T 37 0.01 //y'-value of free-surface turbulence BC
W 22 -9.81

References

[1] M. L. Rocca, G. Sciortino, M. A. Boniforti, Interfacial gravity waves in a two-fluid system, Fluid Dynamics Research 30 (1) (2002) 31.
URL http://stacks.iop.org/1873-7005/30/i=1/a=A04

[2] M. La Rocca, G. Sciortino, C. Adduce, M. Boniforti, Experimental and theoretical investigation on the sloshing of a two-liquid system with free surface, Physics of Fluids (1994-present) 17 (6) (2005) 062101.

[3] R. A. Ibrahim, Liquid sloshing dynamics: theory and applications, Cambridge University Press, 2005.

[4] O. M. Faltinsen, A. N. Timokha, Sloshing, Cambridge University Press, 2009.

[5] H. A. Olsen, K. Johnsen, Nonlinear sloshing in rectangular tanks. A pilot study on the applicability of analytical models.

[6] D. Peregrine, I. Svendsen, Spilling breakers, bores, and hydraulic jumps, Coastal Engineering Proceedings 1 (16).

[7] V. Armenio, M. La Rocca, On the analysis of sloshing of water in rectangular containers: numerical study and experimental validation, Ocean Engineering 23 (8) (1996) 705–739.

[8] M. La Rocca, G. Sciortino, M. A. Boniforti, A fully nonlinear model for sloshing in a rotating container, Fluid Dynamics Research 27 (1) (2000) 23.

[9] P. Mele, V. Armenio, Variational approach to the problem of sloshing in a moving container, Journal of Theoretical and Applied Fluid Mechanics 1 (1997) 280–310.

[10] J. Gómez-Goñi, C. A. Garrido-Mendoza, J. L. Cercós, L. González, Two phase analysis of sloshing in a rectangular container with volume of fluid (VOF) methods, Ocean Engineering 73 (2013) 208–212.
[11] M. Ansari, R. Firouz-Abadi, M. Ghasemi, Two phase modal analysis of nonlinear sloshing in a rectangular container, Ocean Engineering 38 (11) (2011) 1277–1282.
[12] W. Bai, X. Liu, C. Koh, Numerical study of violent lng sloshing induced by realistic ship motions using level set method, Ocean Engineering 97 (2015) 100–113.
[13] Y. Zhao, H.-C. Chen, Numerical simulation of 3D sloshing flow in partially filled lng tank using a coupled level-set and volume-of-fluid method, Ocean Engineering 104 (2015) 10–30.
[14] D. Liu, P. Lin, A numerical study of three-dimensional liquid sloshing in tanks, Journal of Computational Physics 227 (8) (2008) 3921–3939.
[15] A. S. Iglesias, L. P. Rojas, R. Z. Rodríguez, Simulation of anti-roll tanks and sloshing type problems with smoothed particle hydrodynamics, Ocean Engineering 31 (8) (2004) 1169–1192.
[16] B. Bouscasse, M. Antuono, A. Colagrossi, C. Lugni, Numerical and experimental investigation of nonlinear shallow water sloshing, International Journal of Nonlinear Sciences and Numerical Simulation 14 (2) (2013) 123–138.
[17] L. Delorme, A. Colagrossi, A. Souto-Iglesias, R. Zamora-Rodriguez, E. Botia-Vera, A set of canonical problems in sloshing, part i: Pressure field in forced rollcomparison between experimental results and SPH, Ocean Engineering 36 (2) (2009) 168–178.
[18] G. Bulian, A. Souto Iglesias, L. Delorme, E. Botia Vera, Smoothed particle hydrodynamics (SPH) simulation of a tuned liquid damper (TLD) with angular motion., Journal of Hydraulic Research 48 (Spécia) (2010) 28–39.
[19] H. Bihs, A. Kamath, M. A. Chella, A. Aggarwal, Ø. A. Arntsen, A new level set numerical wave tank with improved density interpolation for complex wave hydrodynamics, Computers & Fluids 140 (2016) 191–208.
[20] H. Bihs, REEF3D, User Guide (2016).
URL https://reef3d.files.wordpress.com/2012/05/reef3d-userguide_16-11.pdf
[21] M. A. Chella, H. Bihs, D. Myrhaug, M. Muskulus, Breaking characteristics and geometric properties of spilling breakers over slopes, Coastal Engineering 95 (2015) 4–19.
[22] A. Kamath, H. Bihs, Ø. A. Arntsen, Numerical investigations of the hydrodynamics of an oscillating water column device, Ocean Engineering 102 (2015) 40–50.
[23] M. S. Afzal, H. Bihs, A. Kamath, Ø. A. Arntsen, Three-dimensional numerical modeling of pier scour under current and waves using level-set method, Journal of Offshore Mechanics and Arctic Engineering 137 (3) (2015) 032001.
[24] D. Wilcox, Turbulence Modeling for CFD, DCW Industries, Incorporated, 1994.
URL https://books.google.com/books?id=VwlRAAAAMAAJ
[25] D. C. Wilcox, Reassessment of the scale-determining equation for advanced turbulence models, AIAA journal 26 (11) (1988) 1299–1310.
[26] F. R. Menter, Two-equation eddy-viscosity turbulence models for engineering applications, AIAA journal 32 (8) (1994) 1598–1605.
[27] P. A. Durbin, Limiters and wall treatments in applied turbulence modeling, Fluid Dynamics Research 41 (1) (2009) 012203.
URL http://stacks.iop.org/1873-7005/41/i=1/a=012203
[28] H. Schlichting, Boundary-layer theory, McGraw-Hill Book Company, 1979.
[29] D. Naot, W. Rodi, Calculation of secondary currents in channel flow, Journal of the Hydraulics Division 108 (8) (1982) 948–968.
[30] M. Hossain, W. Rodi, Mathematical modelling of vertical mixing in stratified channel flow, in: Proceedings of the 2nd Symposium on Stratified Flows, 1980, pp. 280–290.
[31] S. Osher, J. A. Sethian, Fronts propagating with curvature-dependent speed: algorithms based on hamilton-jacobi formulations, Journal of Computational Physics 79 (1) (1988) 12–49.
[32] M. Sussman, P. Smereka, S. Osher, A level set approach for computing solutions to incompressible two-phase flow, Journal of Computational Physics 114 (1) (1994) 146–159.
[33] D. Peng, B. Merriman, S. Osher, H. Zhao, M. Kang, A PDE-based fast local level set method, Journal of Computational Physics 155 (2) (1999) 410–438.
[34] R. Nourgaliev, S. Wiri, N. Dinh, T. Theofanous, On improving mass conservation of level set by reducing spatial discretization errors, International journal of multiphase flow 31 (12) (2005) 1329–1336.
[35] M. Sussman, E. Fatemi, P. Smereka, S. Osher, An improved level set method for incompressible two-phase flows, Computers & Fluids 27 (5) (1998) 663–680.
[36] A. J. Chorin, Numerical solution of the Navier-Stokes equations, Mathematics of Computation 22 (104) (1968) 745–762.
[37] Center for Applied Scientific Computing, Hyper high performance preconditioners - Users Manual (2015).
[38] G. Jiang, C. Shu, Efficient implementation of weighted ENO schemes, Journal of Computational Physics 126 (130) (1996) 202–228.
[39] P. A. Berthelsen, O. M. Faltinsen, A local directional ghost cell approach for incompressible viscous flow problems with irregular boundaries, Journal of computational physics 227 (9) (2008) 4354–4397.
[40] J. Verhagen, L. Van Wijngaarden, Non-linear oscillations of fluid in a container, Journal of Fluid Mechanics 22 (04) (1965) 737–751.
[41] R. L. Panton, Incompressible Flow, New Jersey: John Wiley & Sons Inc, 2004.